



Breaking the size limitation of nonadiabatic molecular dynamics in condensed matter systems with local descriptor machine learning

Dongyu Liu^a, Bipeng Wang^b, Yifan Wu^c, Andrey S. Vasenko^{a,d,1}, and Oleg V. Prezhdo^{c,e,f,1}

Affiliations are included on p. 7.

Edited by Juan de Pablo, The University of Chicago, Chicago, IL; received February 19, 2024; accepted August 2, 2024

Nonadiabatic molecular dynamics (NA-MD) is a powerful tool to model far-from-equilibrium processes, such as photochemical reactions and charge transport. NA-MD application to condensed phase has drawn tremendous attention recently for development of next-generation energy and optoelectronic materials. Studies of condensed matter allow one to employ efficient computational tools, such as density functional theory (DFT) and classical path approximation (CPA). Still, system size and simulation timescale are strongly limited by costly *ab initio* calculations of electronic energies, forces, and NA couplings. We resolve the limitations by developing a fully machine learning (ML) approach in which all the above properties are obtained using neural networks based on local descriptors. The ML models correlate the target properties for NA-MD, implemented with DFT and CPA, directly to the system structure. Trained on small systems, the neural networks are applied to large systems and long timescales, extending NA-MD capabilities by orders of magnitude. We demonstrate the approach with dependence of charge trapping and recombination on defect concentration in MoS₂. Defects provide the main mechanism of charge losses, resulting in performance degradation. Charge trapping slows with decreasing defect concentration; however, recombination exhibits complex dependence, conditional on whether it occurs between free or trapped charges, and relative concentrations of carriers and defects. Delocalized shallow traps can become localized with increasing temperature, changing trapping and recombination behavior. Completely based on ML, the approach bridges the gap between theoretical models and realistic experimental conditions and enables NA-MD on thousand-atom systems and many nanoseconds.

theoretical chemistry | machine learning | quantum dynamics

Excited state dynamics play key roles in numerous photophysical and photochemical phenomena involving nonequilibrium processes initiated by absorption of a photon, an injection of a charge, or an energetic chemical event and form the basis of many modern applications (1–4). Examples include solar energy utilization (5–7), optoelectronic devices (8–10), novel chemistries (11, 12), catalysis (13–15), imaging and biosensing (15–18), superconductors (19, 20), superfluids (21), and quantum information processing (22). Nonadiabatic (NA) molecular dynamics (MD) is an efficient approach for modeling coupled electronic and atomic degrees of freedom that evolve far from equilibrium. It mimics nature and time-resolved optical experiments in the most direct way, at the atomistic level, and in the time domain (23–26). In solar energy applications, electronics, and optoelectronics, productive processes, such as charge and energy transfer, or breaking and formation of chemical bonds, compete with charge and energy losses. NA-MD provides essential insights needed to steer excited state dynamics in the desired directions and to mitigate the detrimental effects (27–29). NA-MD needs input from time-consuming electronic structure calculations, which limit the method to systems composed of hundreds of atoms and picosecond timescales, if performed at an *ab initio* level. In many cases, larger simulation models and longer simulation times are desired in order to mimic realistic processes (24). Examples include twisted bilayer graphene and transition metal dichalcogenides that exhibit unique electronic and transport properties (30–32) and grain boundaries and interfaces that cause charge and energy losses in perovskite solar cells (33, 34). Atomistic models of such systems are too computationally expensive for time-domain *ab initio* calculations, and simplifications are essential. Breaking the size and timescale limitations of NA-MD is urgent, and machine learning (ML) represents a particularly promising direction (35–37).

Significance

Far-from-equilibrium processes underlie most modern technologies, ranging from solar energy harvesting and utilization to electronics and optoelectronics, imaging and sensing, quantum information processing, and medical therapies. Atomistic time-domain modeling of these processes reveals key mechanisms allowing one to control the flow of energy, charge, and information. Nonadiabatic molecular dynamics provides means to achieve this goal; however, only simplified small systems can be studied in present. We apply modern machine learning tools and develop a methodology that increases system size and simulation timescale by orders of magnitude. As an example, we demonstrate that charge carrier losses in modern materials have a nontrivial dependence on defect concentration under realistic conditions.

Author contributions: D.L., A.S.V., and O.V.P. designed research; D.L., B.W., and Y.W. performed research; D.L., B.W., Y.W., A.S.V., and O.V.P. analyzed data; and D.L., A.S.V., and O.V.P. wrote the paper.

The authors declare no competing interest.

This article is a PNAS Direct Submission.

Copyright © 2024 the Author(s). Published by PNAS. This article is distributed under [Creative Commons Attribution-NonCommercial-NoDerivatives License 4.0 \(CC BY-NC-ND\)](#).

¹To whom correspondence may be addressed. Email: avasenko@hse.ru or prezhdo@usc.edu.

This article contains supporting information online at <https://www.pnas.org/lookup/suppl/doi:10.1073/pnas.2403497121/-DCSupplemental>.

Published August 30, 2024.

NA-MD simulations generally require calculations of nuclear gradients for excited states and NA couplings (NACs) along MD trajectories (23, 38). Thermal fluctuations in condensed phase and nanoscale systems often dominate structural evolution, allowing one to replace expensive excited state calculations by much more affordable ground-state calculations, according to the classical path approximation (CPA) (39, 40). Still, the cost of *ab initio* methods is high. Density functional theory (DFT) is widely used to obtain ground-state electronic properties for a given system geometry. DFT becomes expensive as the system size and MD trajectory length grow. To address this issue, ML models of force fields (FF) (41) and electronic Hamiltonians (31, 42) can be developed using DFT data as training sets to obtain the results with *ab initio* accuracy but at a much lower computational cost. ML models based on local structural descriptors decompose target properties, such as energy, force, and electronic off-diagonal coupling, into atomic contributions, which can be trained with small systems and scaled up to large systems. This feature is highly promising for condensed matter systems because many collective phenomena require large atomistic models and generating *ab initio* training sets for large models is unaffordable. Although many global properties, such as the NAC, are difficult to capture by local descriptors, most of them have analytic relationships with basic interatomic interactions which can be inferred from local configurations by ML. Therefore, development of NA-MD methodologies based on appropriate local descriptors is a promising route to avoid costly *ab initio* calculations and enable investigations of excited state dynamics in complicated systems.

In this work, we develop a fully ML-based approach for performing NA-MD simulations in condensed phase and nanoscale systems composed of thousands of atoms over nanosecond timescales. The methodology is inspired by the ML tools for generation of ML-FFs to perform MD (43) and parameterization of electronic Hamiltonian to obtain electronic state energies and wavefunctions (31), which are sufficient to replace the ground-state *ab initio* calculations for NA-MD within the CPA. We develop means to obtain the NAC within the ML framework and use our group's ML techniques to interpolate NACs over large time intervals (35, 36). We train the ML models for the fundamental properties needed for NA-MD on small model systems and generate the properties for large realistic systems. The ML data are used as input to our group's sophisticated and efficient NA-MD approaches designed to model complex excited state processes (23, 39, 40, 44). We systematically test the developed technique by investigating the dependence of charge carrier trapping and recombination dynamics in a modern material, MoS₂, on concentration of the most common defect, sulfur vacancy. Such an investigation is challenging due to computational limitations on the system size. Defect concentration is the key characteristic of semiconductor quality in a broad range of applications. Typically, defects should be avoided, as they limit carrier mobility and lifetime. However, the practical cost of eliminating defects is high and increases rapidly with material purity. In other cases, defects are introduced on purpose to manipulate optical response (45), pin excitons (46), facilitate charge separation (47), create photo- and electrocatalytic sites (48), etc. Using the developed approach, we demonstrate that charge trapping slows down with decreasing defect concentration. However, charge recombination rate may or may not show concentration dependence, conditional on whether the recombination occurs between free and trapped charges or trapped charges. Delocalized shallow traps can become localized at increased temperature, changing the defect concentration dependence. Compared to *ab initio* NA-MD, the fully ML-based NA-MD approach errs by about 10%, while the

calculation cost is decreased by orders of magnitude. The error is negligible for NA-MD accuracy due to multiple approximations involved (49) and is much smaller than experimental uncertainties. The local descriptor-based ML NA-MD simulations can accurately and efficiently replace the *ab initio* NA-MD calculations, enabling one to investigate complex phenomena in large systems and over long timescales.

Results

Framework of ML-Based NA-MD Simulation. In NA-MD, electrons are treated quantum mechanically, while atomic vibrational motions are classical or semiclassical. Hence, NA-MD simulations combine multiple methodologies needed to perform classical MD, to calculate electronic state energies, wavefunctions, and state-to-state NA and Coulomb couplings, as well as to evolve the mixed quantum-classical system (23, 38, 50). The developed methodology combines ML-FFs, as implemented in DeepMD (51) and ML Hamiltonian (ML-H) of DeepH (31), with decoherence-induced surface hopping (DISH) (52), as implemented in Pyxaid software (39, 40). We augment the DeepH (31) approach to calculate the NAC, which required modifying and tuning the neural network to make the results stable with respect to changes in system geometry and calculation of overlap matrix elements (39). ML models of the electronic state energies and NAC matrix elements developed in our group (35, 36) can be used to interpolate these properties over long time intervals to reduce the cost of the ML-H calculations. This capability is not employed in present, to provide a more rigorous comparison to *ab initio* NA-MD. The ML models are trained to predict the interatomic forces and Hamiltonian matrix elements based on local structure, as illustrated in Fig. 1A. The ML models can be used in extended systems without size limitations. The Hamiltonian matrices defined in a local basis ($\{\phi_i\}$) are diagonalized to produce delocalized molecular orbitals ($\{\psi_i\}$), orbital energies ($\{\epsilon_i\}$), and NACs ($\{d_{ij}\}$) (39).

Fig. 1B displays the workflow of calculating the NA-MD input data with the ML models. ML-FF provides atomic force (F) to update atomic positions (R) and velocities (v) at the next timestep of MD. The MD structure is processed with ML-H to obtain $\{\epsilon_i\}$ and $\{\psi_i\}$. $\{\epsilon_i\}$ give excitation energies at a given timestep, and $\{\psi_i\}$ at adjacent timesteps are used for NAC ($\{d_{ij}\}$) calculations. The combination of the ML-FF and ML-H models allows us to obtain evolving electronic energy levels and NAC along the MD trajectory without *ab initio* calculations. NA-MD uses these data to simulate excited state electron-vibrational dynamics, as illustrated in Fig. 1C. Atomic motions affect energy levels. The reduced energy differences lead to strong NAC between the electronic states, and transitions are more likely to occur. NA-MD simulates the population change in this period, which provides quantum mechanical information on excited state electronic processes, such as charge carrier trapping and recombination.

The methodology is applied to and tested with charge carrier trapping and recombination processes in defective single-layer MoS₂ with sulfur vacancies. MoS₂ is a two-dimensional semiconductor with promising electronic and optoelectronic applications. It has a suitable bandgap and good theoretical carrier mobility, but experimental samples show much lower mobility because of impurities and defects (53). Sulfur vacancy is reported as the dominant defect in MoS₂ (54). It introduces trap states in the bandgap, accelerating charge trapping and electron-hole recombination (55). We demonstrate that, in the testing system containing 107 atoms, the ML-H model can properly reproduce the energy level differences and NACs compared to the DFT calculations, and the trajectories obtained with ML-FF exhibit similar distributions of

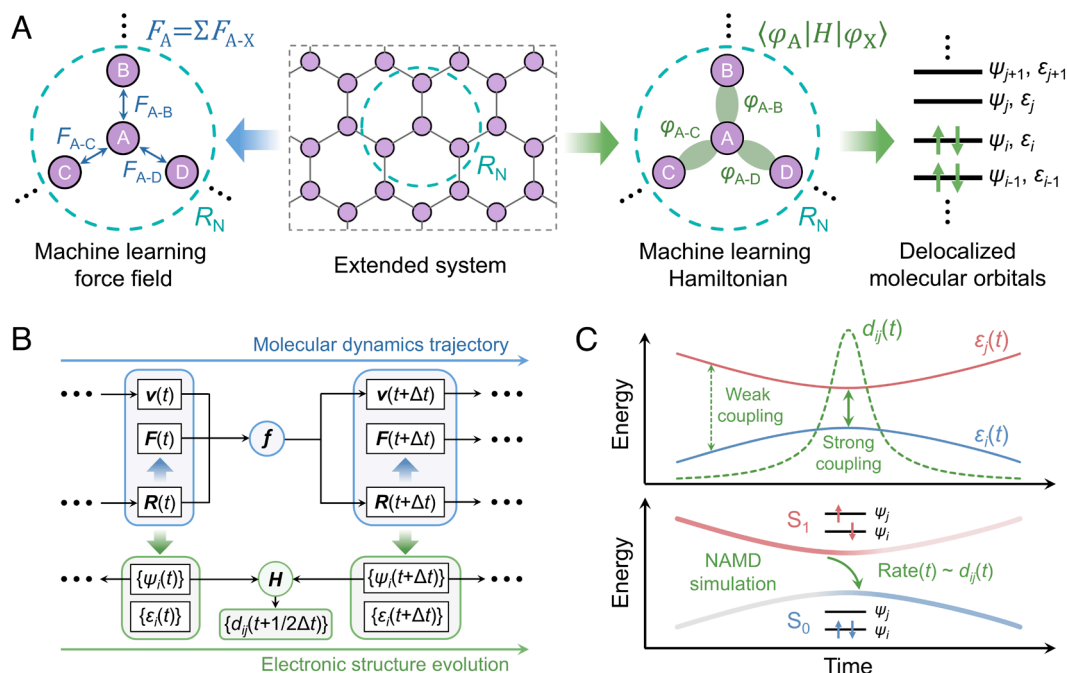


Fig. 1. Overview of NA-MD simulations with local descriptor ML models. (A) ML predictions based on local structure in extended systems. R_N is the neighborhood cutoff radius. Hamiltonian matrices $H_{ij} = \langle \phi_i | H | \phi_j \rangle$ are diagonalized to obtain electronic wavefunctions, $\{\psi_i\}$, and energy levels, $\{\epsilon_i\}$. (B) Workflow of generating NA-MD input with ML models. The atomic force (F) from the ML-FF is used to update the atomic position (R) and velocity (v). $\{\epsilon_i\}$ and $\{\psi_i\}$ from the ML-H are used to calculate excitation energies and NAC, $d_{ij} = \psi_i | \frac{\partial}{\partial t} | \psi_j$. (C) Scheme of evolution of energy levels and NAC along a MD trajectory and electronic transition from ψ_j to ψ_i in NA-MD simulation.

these two results compared to the trajectories from *ab initio* MD (AI-MD) simulations. Then, we apply the developed approach to 431 and 971 atom systems and establish important and unique insights into defect density dependence on charge carrier trapping and recombination in semiconductors.

Calculation of NA-MD Electronic Hamiltonian with ML. We first verify the accuracy of ML-H in producing excited state energies and NACs. Fig. 2A shows the structure of defective single-layer

MoS₂ with a sulfur vacancy. The density of states (DOS) is plotted in Fig. 2B. We use a 6×6 supercell to avoid interaction between sulfur vacancies in adjacent cells. The properties of the supercell can be related to the properties of the unit cell by zone folding (30, 56). The sulfur vacancy introduces one occupied state (trap 1) slightly above the valence band maximum (VBM) and two unoccupied states (traps 2 and 3) deep inside the bandgap, relatively close to the conduction band minimum (CBM) (57). Once an electron is excited to the CB and a hole is generated

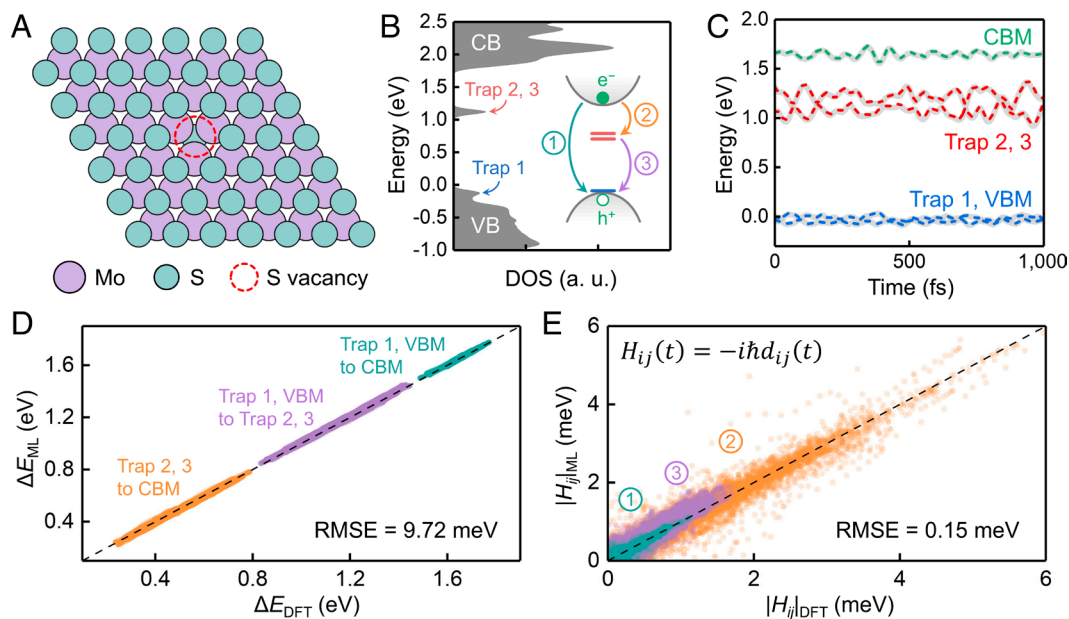


Fig. 2. Validation of ML-H for electronic structure. (A) Top view of the simulation cell. (B) Density of states (DOS) of the defective MoS₂. The inset illustrates direct, ①, and trap-assisted, ② + ③, carrier recombination between conduction band (CB) and valence band (VB). (C) Evolution of energy levels in a 1 ps AI-MD trajectory. Gray lines are from DFT and color lines are from ML-H. The energy of trap 1 at the first step is set to zero. (D) Comparison of electronic energy gaps obtained with DFT and ML-H. (E) Comparison of absolute NAC matrix elements from DFT and ML-H. The data are taken from a 6 ps AI-MD trajectory with a 1 fs timestep.

in the VB, the charges relax to the band edges, i.e., CBM and VBM, very fast and then go through interband recombination. The carriers can go through direct CBM-VBM recombination (①) or trap-assisted recombination (② + ③). Since traps 2 and 3, as well as trap 1 and VBM are nearly degenerate, transitions between these state pairs are very easy, and the populations of these states are combined in the subsequent analysis.

We use a 6 ps AI-MD trajectory to sample system behavior in the atomic phase space. Fig. 2C shows evolution of energy levels of the CBM, VBM, and trap 1, 2, and 3 states in a representative 1 ps trajectory. The gray lines are from DFT, and the color lines are from ML-H. The ML results agree well with the DFT results, and the overall RMS error (RMSE) in the energy gaps is only 9.27 meV. The entire 6 ps data are displayed in *SI Appendix, Fig. S1*. Fig. 2D compares the energy gaps obtained with DFT and ML. The RMSE below 10 meV is insignificant, as the energy gaps are at the eV magnitude. Fig. 2E compares the NACs. These off-diagonal matrix elements govern transition probabilities between electronic states. In the weak coupling limit, the transition probability is proportion to NAC squared (58). The dependence is more complex if NACs are large. The NAC for process ①, Fig. 2B, is small, indicating that direct CBM-VBM recombination is relatively slow, while the trap-assisted recombination (② + ③) is faster since the corresponding couplings are larger. Therefore, carrier recombination is primarily trap-assisted. The RMSE is only 0.15 meV, which is about one order of magnitude lower than the NAC values themselves. More detailed comparisons can be found in *SI Appendix, Fig. S2*.

Capability of Fully ML-Based NA-MD Simulation. Next, we verify the accuracy of ML-FF in MD trajectory sampling. MD trajectories generated with the ML-FF should reproduce structural fluctuations in the system occurring in AI-MD. We obtain another 6 ps MD trajectory with the ML-FF and calculate the electronic properties along the trajectory with ML-H. Thus, we compare distributions of the electronic energy gaps and NACs obtained

fully ab initio, i.e., using ab initio DFT trajectory and DFT electronic structure, and fully ML, i.e., with ML-FF trajectory and ML-H electronic structure. Fig. 3A shows the probability distributions of the energy gaps. The peak pairs arise from splitting of the degenerate states during the MD simulation. The fully ML-based results capture properly the fully DFT-based distributions. Comparison of the NAC matrix elements is displayed in Fig. 3B. The NAC values fluctuate around zero, and the fluctuation amplitude is evaluated with RMS values. The differences in the RMS values obtained with ML and DFT are very small, as reported in the figure. Only the NAC for the direct recombination (①) is slightly overestimated by ML. However, this will not affect the overall dynamics since it is dominated by the trap-assisted recombination (② + ③).

Next, we perform NA-MD simulations of the charge trapping and recombination dynamics based on DFT and ML input. The results are shown in Fig. 3C. An electron is promoted from the VBM to the CBM to establish the initial excited state, and the evolution of populations of the VBM, the CBM and the three trap states are calculated to identify the charge trapping and recombination mechanisms and timescales. The population of the mid-gap trap states (traps 2 and 3) increases at the beginning, as the excited electron in the CBM is captured by the traps within hundreds of picoseconds. Subsequently, the trapped electron recombines with the hole at the VBM or trap 1 on a nanosecond timescale. This process constitutes the rate-determining step (RDS) of the overall electron-hole recombination. The ML dynamics is marginally delayed compared with the DFT dynamics, but the relative differences in the populations of the ground and trap states are only 4% and 11% after the 3 ns simulation, Fig. 3C, which is much lower than the NA-MD error (49) and experimental uncertainties.

The simulations employ two ML models, used to obtain independently the ML-FF and the electronic Hamiltonian. To distinguish the impacts of ML-FF and ML-H on the NA-MD simulations, we performed an additional DFT/ML calculation,

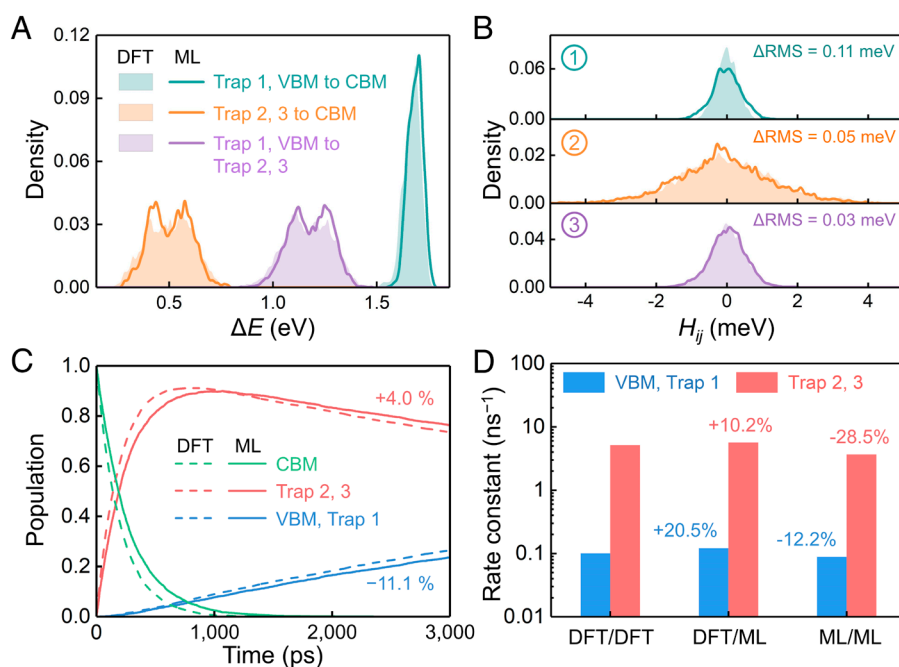


Fig. 3. Validation of ML models for NA-MD simulation. Probability distributions of (A) energy gaps and (B) NACs. The filled regions and solid lines the results fully based on DFT and ML, respectively. (C) Carrier trapping and recombination dynamics based fully on DFT and fully on ML. (D) Carrier trapping and recombination rate constants obtained using different combinations of DFT and ML models for force-field/electronic-Hamiltonian. E.g., DFT/ML means that DFT was used to obtain the MD trajectory, and ML was used to obtain the electronic properties. The values indicate the relative changes compared to the DFT/DFT data.

in which we used the AI-MD trajectory and the ML-H electronic Hamiltonian. Thus, the errors in this calculation arise only from the ML model of the electronic Hamiltonian. The carrier trapping and recombination time constants for the three calculations are compared in Fig. 3D. The values are derived from exponential fits of populations of the mid-gap traps (traps 2 and 3) and the ground state (VBM and trap 1). The details can be found in *SI Appendix, Fig. S3*. The ML-H model tends to overestimate the transition rates, but the ML-FF can compensate for this effect and even slow down the transitions. The errors in the state-to-state transition rate constants, arising from the combination of the ML-H and ML-FF models reach nearly 30%, however, the error in the overall recombination rate is around 10%. These values are fully acceptable given the multiple approximations involved in the NA-MD methodology (49) and experimental errors.

Application to Carrier Dynamics in Transition Metal Dichalcogenides with Defects. We have demonstrated that combining the local descriptor-based ML-FF and ML-H models can properly reproduce the NA-MD results at the ab initio accuracy without performing ab initio calculations. This advantage enables simulations of larger systems, which cannot be treated by ab initio NA-MD, since its computational cost strongly depends on system size. Currently, the system size of ab initio NA-MD based on DFT is limited to few hundred atoms, which is insufficient to describe many realistic systems, e.g., containing point and extended defects, surfaces, interfaces, multiple components, etc. (23). Even for pristine models, the limited system size overestimates the carrier densities compared to the experimental conditions (59). Hence, breaking the size limitations of NA-MD is crucial to reduce the gap between theoretical and experimental studies. Using the developed fully ML approach, we are able to extend the simulation cell from 6×6 to 12×12 and 18×18 unit cells and investigate the size dependence of the carrier recombination dynamics in

defective MoS_2 . The different simulation cell sizes are directly related to defect concentration in experiments.

Fig. 4A shows the probability distributions of energy levels in the three systems of different sizes, and the energy level evolutions are given in *SI Appendix, Fig. S4*. According to statistical mechanics, the relative amplitude of fluctuation is inversely proportional to the root of the number of particles. In the present case, the number of particles corresponds to the number of atoms supporting a particular state. The VBM and CBM fluctuations decrease with increasing system size since these states are delocalized, Fig. 4B. Fluctuations of traps 2 and 3 barely change with system size because these deep traps are localized. Trap 1 exhibits a mixture of these two behaviors since this shallow trap is delocalized at low temperatures and becomes localized as temperature increases, cf. the 2nd and 3rd panels in Fig. 4B. Changes in trap state localization due to thermally induced disorder can have a strong influence on charge carrier trapping and recombination (28).

The energy level fluctuations reflect response of the electronic subsystem to atomic motion, and such response determines the NAC. The coupling between delocalized orbitals is reduced as the system size increases, and the fluctuations are suppressed. The coupling between orbitals localized at the traps is independent of system size. The coupling between localized and delocalized states decreases with system size, as illustrated in Fig. 4C. Fig. 4D shows the relative changes of the RMS NAC in the different systems. The NAC involving delocalized states decreases in proportion to $1/\sqrt{N}$, where N is the number of atoms in each system. This trend is consistent with the dependence of statistical relative fluctuations on the number of particles. In contrast, the couplings between the localized states (i.e., trap 1 and traps 2 and 3) are almost maintained because these states are independent of the system size. The probability distributions of the NACs are given in *SI Appendix, Fig. S5*.

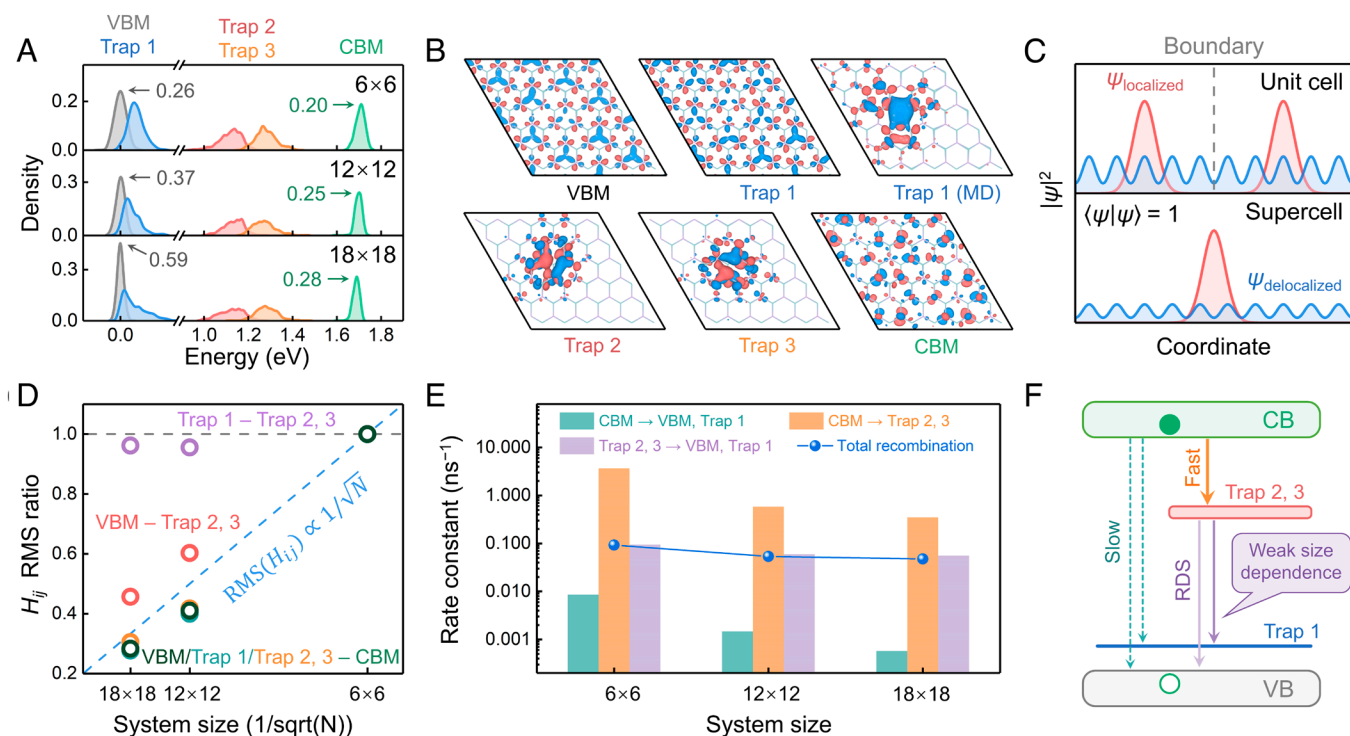


Fig. 4. Dependence of carrier trapping and recombination dynamics on defect concentration, determined by system size. Simulation cells are composed of 6×6 , 12×12 , and 18×18 unit cells. (A) Distributions of VBM, CBM, and trap state energies in the three systems. The average energy of VBM is set to zero. (B) Wavefunctions of these energy levels in the 6×6 system. (C) Dependence of localized and delocalized wavefunctions on simulation cell size. (D) Ratio of H_{ij} RMS in different systems relative to the 6×6 system. (E) Transition rate constants in the three systems. (F) Scheme of carrier trapping and recombination in defective MoS_2 . Electron trapping is fast, and transition from the deep traps 2 and 3 to the shallow trap 1 and the VBM is the rate-determining step (RDS).

The NAC values indicate that the carrier transitions in the defective MoS₂ should possess various size dependences, and the NA-MD simulations are performed to study the size dependence. Fig. 4E displays the transition rate constants in the three systems. The carrier trapping process (CBM → traps 2 and 3) is fast; however, it slows down by an order of magnitude as the system size is increased. The subsequent electron–hole recombination (traps 2 and 3 → VBM and trap 1) is slow and is less affected by the system size because it is contributed by transitions between localized states (traps 2 and 3 → trap 1). The overall carrier recombination follows the trend of the electron–hole recombination step (traps 2 and 3 → VBM and trap 1) that constitutes the bottleneck, without significant size dependence, and the mechanism is illustrated in Fig. 4F. The sulfur vacancies simultaneously introduce occupied and unoccupied trap states in the bandgap, and the trap-assisted path is the main recombination channel in the defective MoS₂. Since the RDS involves transitions between localized trap states with weak size dependence, its rate cannot be efficiently reduced by enlarging the system size. Decreasing the concentration of sulfur vacancies only reduces the number of recombination centers. The simulations show that the charge trapping rate slows down with decreasing defect concentration because it involves transitions between delocalized band states and localized trap states. The charge recombination rate may or may not vary with defect concentration, depending on whether the recombination occurs between free and trapped charges or two trapped charges. The charge trapping and recombination process can also depend on the relative concentrations of carriers and defects, since large number of carriers can saturate all defect sites. The calculation details of the rate constant and more NA-MD simulation results can be found in *SI Appendix, Figs. S6–S8*. These size-dependence results provide important insights into understanding the properties of defects in semiconductor materials. *SI Appendix, Figs. S9 and S10* provide validation of the CPA for the current system.

Experimental Validation. Sulfur vacancies are the most prevalent defects in monolayer MoS₂ prepared by mechanical exfoliation or chemical vapor deposition processes (54), and the defect concentration in as-prepared samples is usually around 10¹³ cm^{−2} (60). The defect concentration in our computational models varies from 3.23 × 10¹³ cm^{−2} to 3.59 × 10¹² cm^{−2}, which is comparable with the experimental conditions. Photoluminescence studies demonstrate that these vacancies lead to localized emission, and the emission peak only appears when the defect concentration is between 10¹³ cm^{−2} and 10¹⁵ cm^{−2} (61). This localized emission is thought to originate from excitons trapped at the vacancy sites studied in our NA-MD simulations (62). This localized transition is size independent, similar to the recombination between the trapped electrons (traps 2 and 3) and holes (trap 1) studied here. The absence of the localized emission at low vacancy concentrations can be attributed to the weak carriers trapping capacity (60). On the other hand, high vacancy concentrations promote the nonradiative recombination of the trapped electrons and holes, as demonstrated here, and quench the photoluminescence process. Although sulfur vacancies are identified as carrier traps and accelerate carrier recombination, both beneficial and detrimental effects on carrier transport are reported (63, 64). The counterintuitive enhancement of carrier transport with increasing vacancy concentration is due to the fact that sulfur vacancies also serve as the hopping sites for carrier transport in MoS₂ (65). Our simulations demonstrate that hole traps at sulfur vacancy sites are shallow, and holes can easily escape into the VB. At the same time, electron traps are highly localized, and increasing the defect concentration reduces the hopping distance for electron transport. The developed ML

methodology can provide further insights into understanding the reported experimental observations.

Discussion

NA-MD provides an efficient approach to investigate excited state dynamics in condensed matter and molecular systems that give rise to optoelectronic and solar energy applications, however, NA-MD has high computational cost. The simulations require sampling of MD trajectories and evaluation of electronic properties along the trajectories. Thousands of ab initio DFT calculations needed for this purpose are unaffordable for systems consisting of more than a few hundred atoms because the computational cost of DFT scales cubically with the number of atoms. However, the performance of solar energy and optoelectronic devices depends on atomistic properties of structures that require large models. Examples include point and extended defects, dopants, impurities, nonstoichiometric compositions, interfaces, grain boundaries, etc. To break the current size limitation of NA-MD, one needs to accelerate the calculation of the input data. NA-MD algorithms themselves are typically computationally efficient, unless very large numbers of electronic states have to be involved (58, 66). In such cases, alternative simulation algorithms are needed (67, 68).

DFT calculations solve the Kohn–Sham equation to obtain the charge density, and this calculation constitutes the computational bottleneck. The charge density is used to calculate the interatomic forces via the Hellmann–Feynman theorem for MD sampling and to construct the Hamiltonian matrix for electronic structure calculations. In order to bypass the time-consuming DFT part, ML can be used to correlate the system structure directly to the target properties. Nevertheless, the ML models need DFT results as training sets, and the system size is still limited by the DFT computational cost. The solution of this problem is provided by local descriptor-based ML models, which can be trained with small systems and applied to large systems. When the system becomes sufficiently large, i.e., thousands of atoms, the diagonalization of the Hamiltonian matrix in the ML-H model creates another bottleneck. Still, ML-H is dramatically faster than ab initio DFT, in particular because the DFT charge density convergence of large systems tends to be difficult. To avoid the Hamiltonian diagonalization one can correlate excitation energies and NAC with structural features directly. Alternatively, one can minimize the number of Hamiltonian diagonalizations by employing time-series interpolation of the electronic properties needed for NA-MD simulation (35, 36).

The performance of our ML-based NA-MD approach depends jointly on the accuracies of the DFT calculations, the ML models, and the NA-MD techniques. DFT is valid for a broad class of systems and processes, nevertheless, it has known limitations, such as description of doubly excited states, charge transfer excitations, and energy gaps in highly correlated materials (69, 70), leading to incorrect excited state energies and unreliable NACs. The latter two issues arise from the electron self-interaction problem that can be alleviated by employing DFT+U or more costly hybrid functionals. Because the ab initio calculations are carried out with small models for generating the training sets for ML, employing advanced DFT functionals is a promising direction. Further, the current method uses the Kohn–Sham description of electronic excitations. The more accurate, linear response time-dependent DFT excitations can be obtained with the ML DFT parameterization. The CPA is based on the assumption that an electronic excitation has little influence on the atomic motion of the system. State-specific forces and trajectories are needed for modeling NA processes with large-scale structural changes, such as photochemical reactions. In

some cases, the CPA can be applied with excited state forces (71). ML models are an interpolation tool and tend to fail in extrapolation tasks. Application of ML requires that system structures used in training are similar to those observed during the finite temperature MD. Note that this requirement is consistent with the CPA. Special methods such as nonadiabatic field (NAF) (72, 73) are needed to accurately describe NA processes involving strongly coupled states in both coupling and asymptotic regions by taking care of the nonadiabatic force contributions. Large systems exhibit many nearly degenerate states because the density of states is proportional to the number of atoms, and strong couplings between these states are expected to greatly influence excited state dynamics. For instance, the carrier cooling in quantum dots is mediated by many states that are nearly degenerate in large models (74), and the unique excitonic properties of twisted bilayer semiconductors originate from the strong interlayer couplings between multiple band edge states (75). Generally, our ML approach serves as a platform for developing innovative NA-MD methods for large-scale condensed matter systems.

Conclusions

To recapitulate, we have developed a fully ML approach to perform NA-MD simulations in large condensed-phase, nanoscale, and molecular systems. Using MoS₂ with a sulfur vacancy as an example, we have extended the system size from 100 atoms to 1000 atoms. We have demonstrated that ML models based on local structural descriptors provide all the input needed to perform NA-MD. The final NA-MD results are close to the ab initio calculations, performed using DFT and CPA, and the errors are within the accuracy of the current NA-MD methodologies and experimental uncertainties. Using the developed approach, we have elucidated the dependence of carrier trapping and recombination in defective MoS₂ on defect concentration. This information is needed for design of optoelectronic and solar energy devices, and

it is challenging to obtain from the conventional DFT/NA-MD investigations. The results show that the charge trapping rate decreases with decreasing defect concentration, while the charge recombination rate may or may not depend on defect concentration, conditional on whether the recombination occurs between free and trapped, or trapped charges, and on the relative concentrations of defects and carriers. The simulations have also shown that the dependence on defect concentration can vary with temperature, in particular, since delocalized shallow traps can become localized due to structure fluctuations. The developed approach provides an orders-of-magnitude speedup of NA-MD simulation compared to the traditional ab initio DFT simulation and can be accelerated further, presenting a valuable tool for modeling and characterization of excited state dynamics in realistic systems.

Methods

The ab initio MD trajectories were obtained with VASP. The ML-FF was trained with DeePMD. OpenMX was used to obtain the ab initio NA-MD Hamiltonian and to train the ML model of the electronic Hamiltonian. The ML model of the electronic Hamiltonian was generated using DeepH. The NA-MD simulations were performed using PYXAID. Simulation details are provided in Supporting Information.

Data, Materials, and Software Availability. All study data are included in the article and/or *SI Appendix*.

ACKNOWLEDGMENTS. This research was supported in part through computational resources of HPC facilities at HSE University. A.S.V. acknowledges support from the Mirror Laboratories Project and the Basic Research Program of the HSE University. O.V.P. acknowledges support of the US NSF, grant CHE-2154367.

Author affiliations: ^aSchool of Electronic Engineering, HSE University, Moscow Institute of Electronics and Mathematics (MIEM), Moscow 123458, Russia; ^bDepartment of Chemical Engineering, University of Southern California, Los Angeles, CA 90089; ^cDepartment of Chemistry, University of Southern California, Los Angeles, CA 90089; ^dDonostia International Physics Center, San Sebastián-Donostia, Euskadi 20018, Spain; ^eDepartment of Physics, University of Southern California, Los Angeles, CA 90089; and ^fDepartment of Astronomy, University of Southern California, Los Angeles, CA 90089

1. K. D. Chapkin *et al.*, Lifetime dynamics of plasmons in the few-atom limit. *Proc. Natl. Acad. Sci. U.S.A.* **115**, 9134–9139 (2018).
2. H. A. Nguyen, I. Srivastava, D. Pan, M. Gruebele, Ultrafast nanometric imaging of energy flow within and between single carbon dots. *Proc. Natl. Acad. Sci. U.S.A.* **118**, e2023083118 (2021).
3. J. S. Higgins *et al.*, Redox conditions correlated with vibronic coupling modulate quantum beats in photosynthetic pigment-protein complexes. *Proc. Natl. Acad. Sci. U.S.A.* **118**, e2112817118 (2021).
4. B. Gu, S. Sun, F. Chen, S. Mukamel, Photoelectron spectroscopy with entangled photons; enhanced spectrottemporal resolution. *Proc. Natl. Acad. Sci. U.S.A.* **120**, e2300541120 (2023).
5. T. Jiang *et al.*, Electronic structure and photophysics of a supermolecular iron complex having a long MLCT-state lifetime and panchromatic absorption. *Proc. Natl. Acad. Sci. U.S.A.* **117**, 20430–20437 (2020).
6. N. P. Gallop *et al.*, Ultrafast vibrational control of organohalide perovskite optoelectronic devices using vibrationally promoted electronic resonance. *Nat. Mater.* **23**, 88–94 (2024).
7. N. Yazdani *et al.*, Coupling to octahedral tilts in halide perovskite nanocrystals induces phonon-mediated attractive interactions between excitons. *Nat. Phys.* **20**, 47–53 (2024).
8. M. Massicotte *et al.*, Picosecond photoreponse in van der Waals heterostructures. *Nat. Nanotechnol.* **11**, 42–46 (2016).
9. A. Wang, X. Jiang, Q. Zheng, H. Petek, J. Zhao, Ultrafast many-body bright-dark exciton transition in anatase TiO₂. *Proc. Natl. Acad. Sci. U.S.A.* **120**, e2307671120 (2023).
10. R. Austin *et al.*, Hot carrier extraction from 2D semiconductor photoelectrodes. *Proc. Natl. Acad. Sci. U.S.A.* **120**, e2220333120 (2023).
11. T.-T. Chen, M. Du, Z. Yang, J. Yuen-Zhou, W. Xiong, Cavity-enabled enhancement of ultrafast intramolecular vibrational redistribution over pseudorotation. *Science* **378**, 790–794 (2022).
12. E. G. Champenois *et al.*, Conformer-specific photochemistry imaged in real space and time. *Science* **374**, 178–182 (2021).
13. R. M. Jay *et al.*, Tracking C-H activation with orbital resolution. *Science* **380**, 955–960 (2023).
14. C. Hu *et al.*, Selective CO₂ reduction to CH₃OH over atomic dual-metal sites embedded in a metal-organic framework with high-energy radiation. *Nat. Commun.* **14**, 4767 (2023).
15. A. M. Wolff *et al.*, Mapping protein dynamics at high spatial resolution with temperature-jump X-ray crystallography. *Nat. Chem.* **15**, 1549–1558 (2023).
16. A. Di Francescantonio *et al.*, All-optical free-space routing of upconverted light by metasurfaces via nonlinear interferometry. *Nat. Nanotechnol.* **19**, 298–305 (2024).
17. S. Mous *et al.*, Dynamics and mechanism of a light-driven chloride pump. *Science* **375**, 845–851 (2022).
18. C. Slavov *et al.*, The interplay between chromophore and protein determines the extended excited state dynamics in a single-domain phytochrome. *Proc. Natl. Acad. Sci. U.S.A.* **117**, 16356–16362 (2020).
19. S. Wandel *et al.*, Enhanced charge density wave coherence in a light-quenched, high-temperature superconductor. *Science* **376**, 860–864 (2022).
20. E. Wang *et al.*, Superconducting nonlinear transport in optically driven high-temperature K₃C₆₀. *Nat. Commun.* **14**, 7233 (2023).
21. A. A. Milner, P. C. E. Stamp, V. Milner, Ultrafast nonequilibrium dynamics of rotons in superfluid helium. *Proc. Natl. Acad. Sci. U.S.A.* **120**, e2303231120 (2023).
22. A. Zong, B. R. Nebgen, S.-C. Lin, J. A. Spies, M. Zuerch, Emerging ultrafast techniques for studying quantum materials. *Nat. Rev. Mater.* **8**, 224–240 (2023).
23. O. V. Prezhdo, Modeling non-adiabatic dynamics in nanoscale and condensed matter systems. *Acc. Chem. Res.* **54**, 4239–4249 (2021).
24. T. R. Nelson, S. Fernandez-Alberti, S. Tretiak, Modeling excited-state molecular dynamics beyond the Born-Oppenheimer regime. *Nat. Comput. Sci.* **2**, 689–692 (2022).
25. Z. Zheng *et al.*, Ab initio real-time quantum dynamics of charge carriers in momentum space. *Nat. Comput. Sci.* **3**, 532–541 (2023).
26. S. Hammes-Schiffer, Exploring proton-coupled electron transfer at multiple scales. *Nat. Comput. Sci.* **3**, 291–300 (2023).
27. R. Shi, W.-H. Fang, A. S. Vasenko, R. Long, O. V. Prezhdo, Efficient passivation of DY center in CH₃NH₂PbBr₃ by chlorine: Quantum molecular dynamics. *Nano Res.* **15**, 2112–2122 (2022).
28. R. Shi *et al.*, Structural disorder in higher-temperature phases increases charge carrier lifetimes in metal halide perovskites. *J. Am. Chem. Soc.* **144**, 19137–19149 (2022).
29. S. Agrawal, A. S. Vasenko, D. J. Trivedi, O. V. Prezhdo, Charge carrier nonadiabatic dynamics in non-metal doped graphitic carbon nitride. *J. Chem. Phys.* **156**, 094702 (2022).
30. Y. Zhu, W.-H. Fang, A. Rubio, R. Long, O. V. Prezhdo, The twist angle has weak influence on charge separation and strong influence on recombination in the MoS₂/WS₂ bilayer: Ab initio quantum dynamics. *J. Mater. Chem. A* **10**, 8324–8333 (2022).
31. H. Li *et al.*, Deep-learning density functional theory Hamiltonian for efficient ab initio electronic-structure calculation. *Nat. Comput. Sci.* **2**, 367–377 (2022).
32. H. Li *et al.*, Deep-learning electronic-structure calculation of magnetic superstructures. *Nat. Comput. Sci.* **3**, 321–327 (2023).
33. Z. Ni *et al.*, High grain boundary recombination velocity in polycrystalline metal halide perovskites. *Sci. Adv.* **8**, eabq8345 (2022).
34. C. M. Wolff, P. Caprioglio, M. Stollerfoht, D. Neher, Nonradiative recombination in perovskite solar cells: The role of interfaces. *Adv. Mater.* **31**, 1902762 (2019).

35. B. Wang, W. Chu, A. Tkatchenko, O. V. Prezhdo, Interpolating nonadiabatic molecular dynamics Hamiltonian with artificial neural networks. *J. Phys. Chem. Lett.* **12**, 6070–6077 (2021).
36. B. Wang, W. Chu, O. V. Prezhdo, Interpolating nonadiabatic molecular dynamics Hamiltonian with inverse fast Fourier transform. *J. Phys. Chem. Lett.* **13**, 331–338 (2022).
37. D. Liu, Y. Wu, A. S. Vasenko, O. V. Prezhdo, Grain boundary sliding and distortion on a nanosecond timescale induce trap states in CsPbBr₃: Ab initio investigation with machine learning force field. *Nanoscale* **15**, 285–293 (2023).
38. Q. Zheng *et al.*, Ab initio nonadiabatic molecular dynamics investigations on the excited carriers in condensed matter systems. *WIREs Comput. Mol. Sci.* **9**, e1411 (2019).
39. A. V. Akimov, O. V. Prezhdo, The PYXAID program for non-adiabatic molecular dynamics in condensed matter systems. *J. Chem. Theory Comput.* **9**, 4959–4972 (2013).
40. A. V. Akimov, O. V. Prezhdo, Advanced capabilities of the PYXAID program: Integration schemes, decoherence effects, multiexcitonic states, and field-matter interaction. *J. Chem. Theory Comput.* **10**, 789–804 (2014).
41. O. T. Unke *et al.*, Machine learning force fields. *Chem. Rev.* **121**, 10142–10186 (2021).
42. G. Zhou, N. Lubbers, K. Barros, S. Tretiak, B. Nebgen, Deep learning of dynamically responsive chemical Hamiltonians with semiempirical quantum mechanics. *Proc. Natl. Acad. Sci. U.S.A.* **119**, e2120333119 (2022).
43. L. Zhang, J. Han, H. Wang, R. Car, W. E, Deep potential molecular dynamics: A scalable model with the accuracy of quantum mechanics. *Phys. Rev. Lett.* **120**, 143001 (2018).
44. L. Wang, A. Akimov, O. V. Prezhdo, Recent progress in surface hopping: 2011–2015. *J. Phys. Chem. Lett.* **7**, 2100–2112 (2016).
45. J. P. Mailoa *et al.*, Room-temperature sub-band gap optoelectronic response of hyperdoped silicon. *Nat. Commun.* **5**, 3011 (2014).
46. Y. J. Zheng *et al.*, Point defects and localized excitons in 2D WSe₂. *ACS Nano* **13**, 6050–6059 (2019).
47. R. Sarkar *et al.*, Common defects accelerate charge separation and reduce recombination in CNT/molecule composites: Atomistic quantum dynamics. *J. Am. Chem. Soc.* **143**, 6649–6656 (2021).
48. H. Wang *et al.*, Highly active deficient ternary sulfide photoanode for photoelectrochemical water splitting. *Nat. Commun.* **11**, 3078 (2020).
49. W. Li, A. V. Akimov, How good is the vibronic Hamiltonian repetition approach for long-time nonadiabatic molecular dynamics? *J. Phys. Chem. Lett.* **13**, 9688–9694 (2022).
50. T. R. Nelson *et al.*, Non-adiabatic excited-state molecular dynamics: Theory and applications for modeling photophysics in extended molecular materials. *Chem. Rev.* **120**, 2215–2287 (2020).
51. H. Wang, L. Zhang, J. Han, W. E, DeePMD-kit: A deep learning package for many-body potential energy representation and molecular dynamics. *Comput. Phys. Commun.* **228**, 178–184 (2018).
52. H. M. Jaeger, S. Fischer, O. V. Prezhdo, Decoherence-induced surface hopping. *J. Chem. Phys.* **137**, 22A545 (2012).
53. D. Lembke, S. Bertolazzi, A. Kis, Single-layer MoS₂ electronics. *Acc. Chem. Res.* **48**, 100–110 (2015).
54. J. Hong *et al.*, Exploring atomic defects in molybdenum disulfide monolayers. *Nat. Commun.* **6**, 6293 (2015).
55. H. Wang, C. Zhang, F. Rana, Ultrafast dynamics of defect-assisted electron-hole recombination in monolayer MoS₂. *Nano Lett.* **15**, 339–345 (2015).
56. Y. Zhu, O. V. Prezhdo, R. Long, W.-H. Fang, Twist angle-dependent intervalley charge carrier transfer and recombination in bilayer WS₂. *J. Am. Chem. Soc.* **145**, 22826–22835 (2023).
57. M. H. Naik, M. Jain, Substrate screening effects on the quasiparticle band gap and defect charge transition levels in MoS₂. *Phys. Rev. Mater.* **2**, 084002 (2018).
58. K. Hyeon-Deuk, O. V. Prezhdo, Time-domain ab initio study of Auger and phonon-assisted Auger processes in a semiconductor quantum dot. *Nano Lett.* **11**, 1845–1850 (2011).
59. S. Wang *et al.*, Effective lifetime of non-equilibrium carriers in semiconductors from non-adiabatic molecular dynamics simulations. *Nat. Comput. Sci.* **2**, 486–493 (2022).
60. S. Shree *et al.*, High optical quality of MoS₂ monolayers grown by chemical vapor deposition. *2D Mater.* **7**, 015011 (2019).
61. Y. Zhu *et al.*, Room-temperature photoluminescence mediated by sulfur vacancies in 2D molybdenum disulfide. *ACS Nano* **17**, 13545–13553 (2023).
62. E. Mitterreiter *et al.*, The role of chalcogen vacancies for atomic defect emission in MoS₂. *Nat. Commun.* **12**, 3822 (2021).
63. X. Zhang *et al.*, Hidden vacancy benefit in monolayer 2D semiconductors. *Adv. Mater.* **33**, 2007051 (2021).
64. S. Bertolazzi *et al.*, Engineering chemically active defects in monolayer MoS₂ transistors via ion-beam irradiation and their healing via vapor deposition of alkanethiols. *Adv. Mater.* **29**, 1606760 (2017).
65. H. Qiu *et al.*, Hopping transport through defect-induced localized states in molybdenum disulfide. *Nat. Commun.* **4**, 2642 (2013).
66. C. Yan *et al.*, Uncovering the role of hole traps in promoting hole transfer from multiexcitonic quantum dots to molecular acceptors. *ACS Nano* **15**, 2281–2291 (2021).
67. J.-J. Zhou *et al.*, Perturbo: A software package for ab initio electron-phonon interactions, charge transport and ultrafast dynamics. *Comput. Phys. Commun.* **264**, 107970 (2021).
68. Y.-S. Wang, P. Nijjar, X. Zhou, D. I. Bondar, O. V. Prezhdo, Combining Lindblad master equation and surface hopping to evolve distributions of quantum particles. *J. Phys. Chem. B* **124**, 4326–4337 (2020).
69. P. Borlido *et al.*, Large-scale benchmark of exchange–correlation functionals for the determination of electronic band gaps of solids. *J. Chem. Theory Comput.* **15**, 5069–5079 (2019).
70. N. T. Maitra, Double and charge-transfer excitations in time-dependent density functional theory. *Annu. Rev. Phys. Chem.* **73**, 117–140 (2022).
71. C. Cheng, O. V. Prezhdo, R. Long, W.-H. Fang, Photolysis versus photothermolysis of N₂O on a semiconductor surface revealed by nonadiabatic molecular dynamics. *J. Am. Chem. Soc.* **145**, 476–486 (2023).
72. B. Wu, X. He, J. Liu, Nonadiabatic field on quantum phase space: A century after Ehrenfest. *J. Phys. Chem. Lett.* **15**, 644–658 (2024).
73. X. He, X. Cheng, B. Wu, J. Liu, Nonadiabatic field with triangle window functions on quantum phase space. *J. Phys. Chem. Lett.* **15**, 5452–5466 (2024).
74. O. V. Prezhdo, Photoinduced dynamics in semiconductor quantum dots: Insights from time-domain ab initio studies. *Acc. Chem. Res.* **42**, 2005–2016 (2009).
75. Y. Shimazaki *et al.*, Strongly correlated electrons and hybrid excitons in a moiré heterostructure. *Nature* **580**, 472–477 (2020).